Theoretical study of xenon adsorption on UO 2 surfaces

Jack Arayro, Guy Treglia, Fabienne Ribeiro

Theoretical study of xenon adsorption on UO_2 surfaces

Journal of Physics Communications

PAPER

Theoretical study of xenon adsorption on UO_2 surfaces

Jack Arayro[1], Guy Tréglia[2] and Fabienne Ribeiro[1]

[1] Institut de Radioprotection et de Sûreté Nucléaire, IRSN, Bat. 702, C.E. Cadarache, BP3-13115 Saint Paul-Lez-Durance Cedex, France
[2] Aix Marseille Univ, CNRS, CINaM, Centre Interdisciplinaire de Nanosciences de Marseille, Marseille, France

E-mail: fabienne.ribeiro@irsn.fr

Keywords: nuclear materials, interfacial stresses, UO_2, atomistic modelling, fission products

OPEN ACCESS

RECEIVED
16 January 2018

REVISED
28 February 2018

ACCEPTED FOR PUBLICATION
8 March 2018

PUBLISHED
27 March 2018

Abstract

During in-pile operation, fission gases such as xenon are produced and precipitates in nuclear fuel as nano-bubbles, modifying the thermomechanical properties of UO_2 fuel matrix. This work aims at precising the nature and the scope of the xenon—UO_2 matrix interaction. To this end, we present a theoretical study of xenon adsorption on UO_2 surfaces, based on Monte Carlo simulation and semi-empirical interatomic potential. We determine xenon adsorption isotherms on previously relaxed (111) and (100) UO_2 surfaces, and we compare them to the incorporation ones inside an empty box in order to isolate interface effects. A specific attention is given to the microstructure of xenon in these systems. Finally, an analysis of the mechanical properties (pressure and stress profiles near by the surface) is achieved in order to investigate the sensitivity to surface orientation and to get pertinent quantities that will supply micromechanical models at higher scale.

1. Introduction

Uranium dioxide UO_2 is the standard fuel in nuclear pressurized water reactors (PWR). During the reactor operation, the fuel pellets undergo thermal and mechanical stresses. For this reason it is very important to understand the thermomechanical properties of this system both in normal operation conditions and accidental situations (from 300 to 2000 K). During uranium fission reactions, rare gases such as xenon are produced within the fuel pellets. Due to their low solubility, these gases are generally found in bubble shape, from nanometer to micrometer diameters. Due to their impact on the overall behaviour of the fuel rod, fission gases behaviour in oxide fuel has been the focus of attention for decades from both experimental [1–3] and theoretical [4–8] points of view. The internal pressure of the bubbles, particularly in the event of a rapid increase in temperature, is suspected of generating internal stress in the fuel. Evaluating this pressure is a key matter especially for nuclear safety aspects [9]. Usually, the pressure inside the bubbles is determined using either the perfect gas or the van der Waals equations of state. Unfortunately, these expressions are totally unsuited in the temperature and pressure ranges encountered in nuclear fuel intragranular bubbles. Indeed, experimental results indicate that the xenon pressure order of magnitude is of a few GPa in these systems [1, 2]. That is the reason why alternative equations of state have been suggested [7, 8], but they are still not taking into account the Xe-UO_2 interactions at the gas-matrix interface, which implies neglecting confinement effects although they are known to be very significant [5, 6]. Similarly, the pressure inside the fuel matrix is determined through the Laplace's law and using average bubble radius and UO_2 surface tension, without taking into account the Xe-UO_2 interactions.

The present work aims to overpass these limitations by means of atomistic simulations. Indeed, computer simulations have been considered as a new research tool for a better understanding of processes occurring at the atomic scale, but also for processes that could not be observed directly by experimental means. A previous work [10] focused on xenon incorporation in UO_2 nanocavities by mean of GCMC approaches, revealed that xenon adsorption isotherms exhibit an abrupt transition from a dilute phase towards a dense one as a function of increasing chemical potential. Whatever the temperature, the corresponding internal gas pressure values are in agreement with most recent atomistic studies, but definitely prove that mesoscopic models based on gas state

behaviour are totally unsuited and must be changed. In order to have a global physical view of the situation, the next step is now to investigate also, by similar approaches, the pressure inside the matrix.

At the atomic scale, intragranular bubbles take the shape of an octahedron, presenting mainly (111) and (100) facets [3]. Given the complexity of this octahedron stability study, we have simplified the problem by decoupling the various effects. We have previously [11] studied the relaxation process of these surfaces and characterized the resulting UO_2 surface microstructure, as well as the energetic and stress profile in its vicinity. In all cases, it was found that whatever the quantity under consideration is (relaxation, energy, stress), the presence of the surface only affects the outermost layer for the (111) direction, but a more extended region for the (100) one. This result will have important consequences on micromechanical models that should take into account these two different behaviours, for instance by introducing different effective surface thicknesses. The next step of this study is now to extend it to the case of xenon-UO_2 system and to answer the question: what is the stress propagation inside the xenon-UO_2 system and does this propagation depends on the UO_2 surface orientation?

For this purpose, we determine here the adsorption isotherms of xenon on previously relaxed surfaces, and we compare them to the incorporation ones inside an empty box in order to isolate gas-matrix interface effects. A specific attention is given to the microstructure of xenon in these systems. Finally, an analysis of the mechanical properties (pressure and stress profiles near by the surface) is achieved in order to get the pertinent quantities that will supply micromechanical models at higher scale.

2. Methods

2.1. Simulation systems

2.1.1. UO_2 surface modelling

As previously described [6, 10, 11], the system modelled here is xenon atoms in interaction with a network of UO_2, generated by infinitely duplicating the elementary cell in the three space directions. The UO_2 elementary cell is fluorite type and its lattice constant is $a = 0.547$nm as determined experimentally at 296 K [12].

Such structure cannot simply be reduced to a stacking of atomic planes along any direction. Thus, in the (111) direction, the structure can be viewed as a stacking of 'triple layers', made up of O-U-O successive atomic planes. The situation is simpler in the (100) direction along which the structure is an alternate stacking of oxygen and uranium planes.

In practice, we use as a starting point a perfect fluorite structure cell of 2592 atoms ($6 \times 6 \times 6$ supercells), corresponding to a UO_2 volume of about 35 nm^3, and we extend Lz to $Lz = 12a = 6.564$ nm to mimic a surface perpendicular to the Z direction.

2.1.2. Pure xenon

With respect to the pure xenon system (in the absence of UO_2 surfaces), which is used as a reference, we have considered an empty box with fixed dimension $Lx = Ly = Lz = 3.272$ nm duplicated in the three space directions by periodic boundary conditions. The size of this system was chosen such as the cell parameter exceeds $2r_{Xe-Xe}$ ($r_{Xe-Xe} = 1.5$ nm is the range of xenon-xenon interactions) and that the total cell volume is similar to the free volume considered for the two previously mentioned surface situations. It should be noticed that the minimal density variation accessible by our study is bounded by the simulation cell size: $\Delta\rho_{Xe} = \frac{1}{L_x \times L_y \times L_z} = 0.3 \times 10^{26}$ at./m^3. Therefore, the very low density systems (for highly negative chemical potentials) will not be relevant.

2.2. Monte carlo thermostatistic tools

We have separated our study in two successive steps: the first one is to relax the matrix surface in absence of xenon, described in [11], and the second one is to adsorb xenon on the relaxed surface. We have checked the validity of our assumption not to relax the matrix under xenon incorporation by adding in some high density cases post-incorporation relaxation studies, without any changing in the main conclusions. All the simulations are performed by Monte Carlo simulations, in canonical (NVT) ensemble for relaxation steps, and in grand canonical (μ,V,T) ensemble for the incorporation study.

In the canonical ensemble, the only proposed events between a configuration i with energy E_i and a configuration $i + 1$ with energy E_{i+1} are the atom displacements, which are accepted with the probability $P_{i,i+1}$:

$$P_{i,i+1} = e^{-\frac{(E_{i+1} - E_i)}{kT}} \quad (1)$$

with k the Boltzmann constant and T the temperature.

In the grand canonical ensemble two other types of events are proposed, the addition or the removal of one xenon atoms, with the respective probabilities $P^{add}_{i,i+1}$ and $P^{rem}_{i,i+1}$ [13]:

$$P_{i,i+1}^{add} = \frac{V}{\Lambda^3(N_i+1)} e^{-\frac{(E_{i+1}-E_i+\mu)}{kT}} \quad (2)$$

$$P_{i,i+1}^{rem} = \frac{\Lambda^3 N_i}{V} e^{-\frac{(E_{i+1}-E_i-\mu)}{kT}} \quad (3)$$

where N_i is the number of atoms in the configuration i, V the system volume, $\Lambda = \frac{h}{\sqrt{2\pi kTm}}$ the De Broglie wavelength, m the xenon atomic mass, h the Plank constant and μ the fixed chemical potential.

In practice, the type of event is chosen randomly, according to the following distribution: 40% for moves, 30% for additions and 30% for removals. Finally, the displacement vector is randomly chosen too, in a distance range from 0 to 5% of the Xe-Xe equilibrium distance. The Grand Canonical Monte Carlo (GCMC) approach allows us to determine isothermal xenon incorporation curve. The thermodynamic equilibrium is assumed to be reached when the statistical number of created particles equals that of the removed ones, which generally requires more than 3×10^8 proposed steps. Additional Canonical Monte Carlo steps are then achieved to average the physicals quantities of interest (the number of particles N_{Xe}, the xenon pressure P, the system energy E...). Typically, 10 000 configurations each 3000 steps are used, to avoid correlation between consecutive steps.

2.3. Energetic model

Semi-empirical approaches are better adapted here than *ab initio* ones since the present work involves the study of thousands atom systems. In addition, the physical properties of interest, such as mechanical or thermal properties, do not require a precise calculation of the electronic structure.

2.3.1. UO interaction model

There exist a variety of UO_2 effective energetic models in the literature [14–17]. We choose here the Basak potential [18] which accounts for the interactions involved in UO_2 and correctly reproduces macroscopic quantities such as the elastic constants, especially at high temperature and for structures far from the perfect crystal [12, 19]. In addition, this potential reproduces fairly well surface properties, and in particular surface energies for main orientations [20]. Within this potential the total energy E_{tot} is written analytically as a function of the atomic positions, as a sum of an electrostatic term ($E_{Coulomb}$), a Buckingham-Hill (E_{Buck}) and a Morse one (E_{Morse}).

$$E_{tot} = E_{Coulomb} + E_{Buck} + E_{Morse} \quad (4)$$

where $E_{Coulomb}$ is given by:

$$E_{Coulomb} = \sum_i \sum_j \frac{q_i q_j}{4\pi\epsilon_0 r_{ij}} \quad (5)$$

where q_i and q_j are the particle charges for $i, j = O, U$ (with $q_0 = -1.2$ and $q_U = 2.4$ [18]), and r_{ij} the interatomic distances. This term is computed using an usual Ewald summation.

The Buckingham Hill component has the following analytical form:

$$E_{Buck} = \sum_i \sum_j A_{ij} e^{-\frac{r_{ij}}{\rho_{ij}}} - \frac{C_{ij}}{r_{ij}^6} \quad (6)$$

and the Morse component this one:

$$E_{Morse} = \sum_i \sum_j D_{ij}[1 - e^{\beta_{ij}(r_{ij}^* - r_{ij})}]^2 - 1 \quad (7)$$

The parameters A_{ij}, ρ_{ij}, C_{ij}, D_{ij}, β_{ij} and r_{ij}^* used for the previous equations, based on the Basak potential for U-O interactions [21], Grimes one for Xe-UO interactions [16] and modified Brearley potential for Xe-Xe interactions [22, 23], are summarised in table 1.

2.4. Stress profile determination

The symmetric per-atom stress tensor for each i atom is computed through the LAMMPS code following the formula [24]:

$$S_{ab} = -\left(m v_a v_b + \sum_{j>i}^{N} (r_{i_a} - r_{j_a})(f_{ij_b}^p) + \sum_{j>i}^{N} (r_{i_a} - r_{j_a})(f_{ij_b}^c) + K_{space}(r_{i_a f_{i_b}}) \right) \quad (8)$$

where a and b take on values (x, y, z), r_{i_a} is the i-atom position, $f_{ij_b}^p$ is the force resulting from the pairwise interaction (except Coulombic contribution) between the i and j atoms; $f_{ij_b}^c$ is the force resulting from the short range Coulombic interaction between the i and j atoms. K_{space} is the contribution from long-range Coulombic interactions, calculated using the method described in [25] for the Ewald method. In the stress expression, the

Table 1. U-O Basak interaction parameters.

Parameters	O-O	U-U	U-O	XeU	XeXe	XeO
A_{ij} (eV)	1633.67	294.76	693.93	6139.16	4934.10	598.00
C_{ij} (eV·nm^6)	39.50	—	—	718.4	2974.7	1083.8
ρ_{ij} (nm)	0.0327	0.0327	0.0327	0.034	0.036	0.043
D_{ij} (eV)	—	—	0.57745	—	—	—
β_{ij} (nm^{-1})	—	—	16.58	—	—	—
r_{ij}^* (nm)	—	—	0.2369	—	—	—

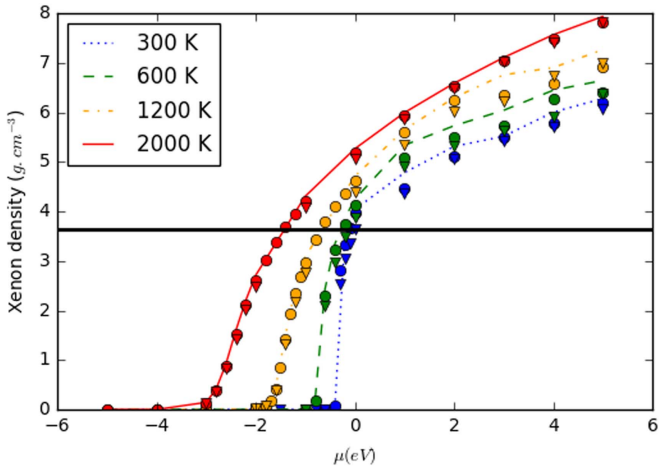

Figure 1. Equilibrium density of xenon incorporated in an empty box as a function of the chemical potential for four different temperatures: 300 K (blue, dotted line), 600 K (green, dash dotted line), 1200 K (yellow, dashed line) and 2000 K (red, solid line). Round markers (respectively triangle) stand for values obtained by incorporation on (111) surface (respectively (100) surface). The horizontal line stands for the value at the triple point in the pure xenon phase diagram.

force term expressed in (8) needs to be divided by the per-atom volume to have unit of stress. However, it is not easy to unambiguously define an individual atomic volume, and we have chosen to keep here this *stress* ∗ *volume* formulation, which leads to use eV unit.

As previously done [11], the off-diagonal S_{xy}, S_{yz} and S_{xz} components of the tensor are found negligible, consistently with no residual shear stress induced by the presence of the surface, therefore they are not represented here. We have also checked that, due to the crystallographic symmetries of the structure, the S_{xx} and S_{yy} components are equal, and we will use the following notation $S_{//} = S_{xx} = S_{yy}$ and $S_{\perp} = S_{zz}$.

These per-atom values are averaged over an hundred configurations generated by LAMMPS Molecular Dynamic at 300 K neglecting the thermal expansion, and they are then averaged in layers perpendicular to the surface to obtain stress profiles.

3. Isothermal xenon adsorption analysis

3.1. Temperature effect

The physical incorporation of xenon inside the previously described systems has been achieved within GCMC, for different chemical potentials and temperatures. The values of explored chemical potentials have been chosen in the characteristic range of the xenon state inside the fuel, namely [−2 eV; 10 eV], taking into account the energy of a xenon atom inside the UO_2 matrix in interstitial (∼20 eV) or vacancy (∼5–10 eV) positions [6, 26, 27]. The temperature range has been chosen to be consistent with the in-pile conditions, and extends from 300 to 2000 K.

Figure 1 represents the corresponding incorporation isotherms with or without UO_2 surfaces. We recover the previous qualitative results of isothermal adsorption in nanobubbles [10]: all curves exhibit the same general behaviour with a first zero or almost zero part followed by a more or less abrupt jump to a new plateau at a critical chemical potential μ_c. This behaviour is characteristic of a phase transition from dilute to condensed system. Both the values of the critical chemical potential μ_c and that of the saturation density ρ_s at the plateau, depend on the temperature:

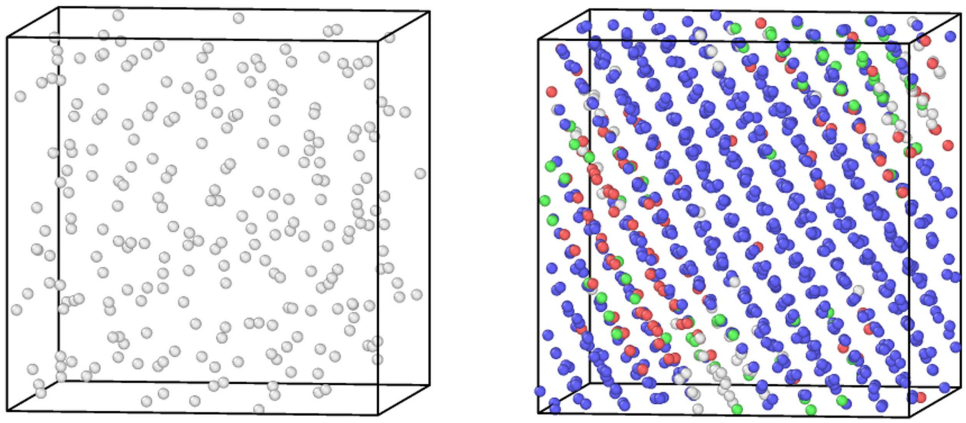

Figure 2. Crystallographic nature of xenon sites incorporated in an empty box at 1200 K for $\mu = -1.4$ eV (left, density = 1.4 g.cm^{-3}) and $\mu = 5$ eV (right, density = 6.9 g.cm^{-3}): BCC in blue, HCP in red, FCC in green, no structure in white.

- at 300 K the xenon saturation density ρ_s corresponds to about 6.5 g.cm^{-3}, which is around twice $\rho_{eq} = 3.6$ g.cm^{-3}, the metallic xenon phase density [28];
- the higher the temperature, the lower μ_c is and the higher ρ_s is. For example, ρ_s increases by about 40 % between 300 and 2000 K. Furthermore, temperature increase smoothes the phase transition. This temperature dependence of ρ_s value is far from being intuitive, and should be related to thermal fluctuations as previously discussed [10].

Based on the comparison of the three system isotherms, the impact of the UO_2 surfaces on the number of adsorbed xenon atoms seems to be negligible in all the temperature range and in almost the whole range of chemical potentials ($\mu < 4$ eV).

3.2. Xenon structuring

3.2.1. Pure xenon

In order to clarify this qualitative description of a diluted/dense phase transition, we have characterized the different obtained microstructures. In all the temperature range the structuring of xenon is very comparable, so that we limit ourselves here to the presentation of the results obtained at 1200 K. In the figure 2, we can observe a very dilute phase at low chemical potential and, on the contrary, a dense phase, which in addition seems to have a crystalline order at high chemical potential.

In order to characterize the nature of this crystalline order, we have analysed the local atomic environments by polyhedral template matching, using the Ovito [29] software. The result is shown in figure 3 in which the evolution of the different atomic populations as a function of the chemical potential is represented for the three isotherms (pure Xe, on UO_2 (100) or (111) surfaces). It can be observed that the condensed phase of xenon is constructed by co-existing close-packed (FCC/HCP) and more open (BCC) phases, which is consistent with the data from the literature [30, 31], although it is difficult to conclude as to a real thermodynamic coexistence between the different structures, or the prevalence of one over the others.

In what concerns the xenon structuring, we can note from the previous figure that it occurs at lower chemical potentials in presence of a surface than in an empty box, and in the former case for a slightly higher chemical potential on a (100) surface than on a (111) surface. Therefore, the UO_2 surface presence seems to facilitate the structuring of the xenon, the (111) surface appearing more efficient in this way, even if it does not impact the number of Xe adsorbed atoms as stated above. We will see in the next section that this will have consequences on mechanical properties.

Xenon BCC phase can be noticed, which could suggest that by preventing the development of this phase, HCP / FCC / BCC competition is no longer as important and no longer interferes with the ordering of the xenon system which oscillates between the different crystal orders.

3.2.2. UO_2 (111) surface effect on Xe adsorption

In order to clarify the UO_2 surface impact on xenon structuring, we carried out a more detailed structural analysis of systems at 1200 K. In the figure 4, which illustrates the distribution of the atoms as a function of their position perpendicularly to the surface for the configuration obtained for $\mu = 4$ eV, we notice that xenon atoms form planes, parallel to the (111) surface and constituted of about the same number of xenon atoms as in the first

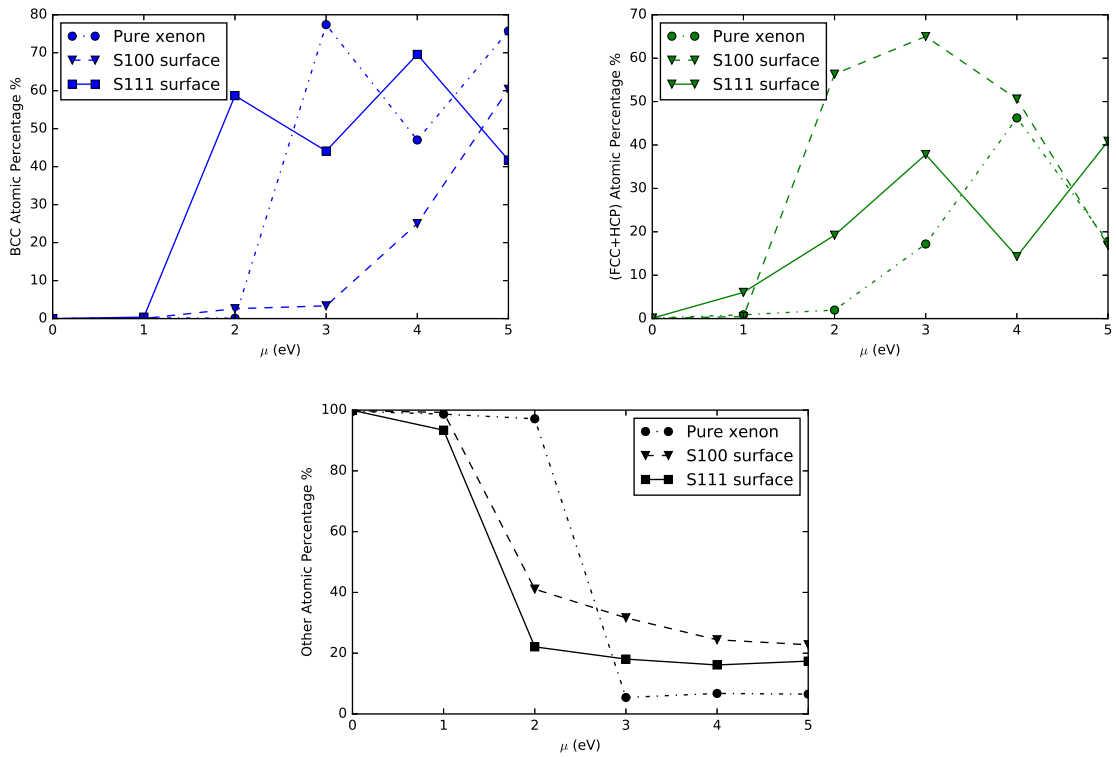

Figure 3. Evolution of the different atomic populations at equilibrium at 1200 K according to the chemical potential, for the three isotherms realized (pure Xe (round markers, dash dotted line), UO_2 (100) surface (triangle markers, dashed line) and (111) surface (square markers, solid line)): BCC in blue, FCC+HCP in green, no structure in black.

oxygen underlayer (coverage $\theta = N_{Xe}/N_O \simeq 1$). This plane structuring is observed for $\mu \geqslant 2$ eV. More precisely, we observe a succession of planes parallel to the (111) surface, regularly distributed at an average distance of 2.9 to 3.0 Å for μ varying between 1 and 4 eV, as illustrated in figure 4. For lower chemical potential, we have also observed the presence of some (one for $\mu = 0$ eV, 3 for $\mu = 1$ eV)) xenon planes in direct vicinity of UO_2 surface, which confirms that the surface presence helps the plane structuring of the xenon. This structuring is consistent with the results of Geng *et al* [32]. As soon as Xe slab structuring is achieved, the distance between this first Xe slab and the last O one is of the some order of magnitude than the Xe-Xe interplane distance and decrease from 3.02 Å ($\mu = 1$ eV) to 2.87 Å ($\mu = 4$ eV).

Further analysis shows that, when the xenon density permits, the first xenon planes (at the interface) have exactly the same number of atoms as the uranium and oxygen planes ($\theta = 1$). From the point of view of structuring, the xenon atoms belonging to these planes assume exactly the same positions as the neighbouring uranium or oxygen atoms (see figure 5), thus indicating a pseudomorphism between the UO_2 planes and those of the adsorbed xenon, which therefore form a hexagonal plane (111). The same pseudomorphism was observed at 300 K for a chemical potential between 2 and 4 eV, at 600 K for a chemical potential between 1 and 4 eV and at 1200 K for a chemical potential of 2 eV. These conditions correspond to xenon density range of 5.6-6.7 g.cm^{-3} (higher than $\rho_{eq} = 3.6$ g.cm^{-3}.)

In these cases, the mean lateral distance between the first nearest neighbours of the Xe $d_{Xe-Xe} = 3.81$ Å is very close to that of the uranium d_{U-U} and the oxygen d_{O-O} of the same plane. This value is less than the distance between the first nearest neighbours of xenon in the FCC and BCC systems at equilibrium at 0 K, which is 4.3 and 4.24 Å, respectively. The xenon is therefore compressed laterally, but less than in the direction perpendicular to the surface (3 Å at 1200 K and $\mu = 2$ eV). A tetragonalization of the xenon structure is thus observed, which tends to compress it even more at the interface (2.8 Å at 1200 K and $\mu = 2$ eV).

The observed pseudomorphism can be seen as the signature of effective lateral interactions (as meditated by the substrate) between xenon atoms, much weaker than the interactions of the latter with the UO_2 substrate atoms. This effect obviously depends on the chemical potential, since an increase of the later induces an increase of the density, which leads to the incorporation of xenon atoms both in and between the planes described above, and then strongly disturbs the scheduling.

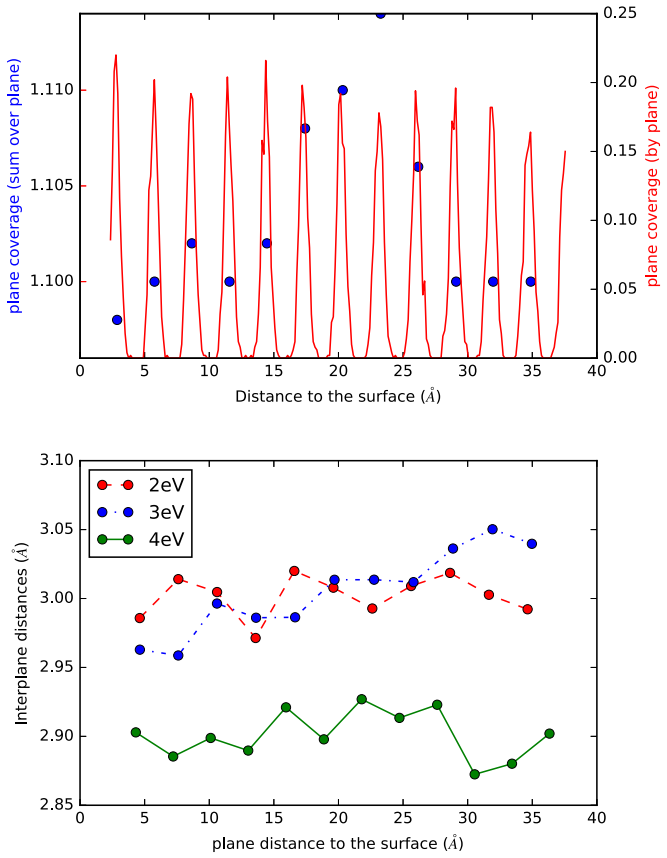

Figure 4. Xe adsorption at 1200 K and $\mu = 4$ eV on (111) UO_2 surface: Xe atomic distribution as a function of the azimuthal position (top), and interplane distance (bottom) for $\mu = 2$ eV (red, dashed line), $\mu = 3$ eV (blue, dash dotted line) and $\mu = 4$ eV (green, solid line). Only half of the slab is shown.

3.2.3. UO_2 (100) surface effect on Xe adsorption

The figure 6 illustrates the distribution of the atoms as a function of their position perpendicularly to the surface for the configuration obtained for $\mu = 4$ eV. As previously on the (111) surface, we observe a succession of planes parallel to the (100) surface, regularly distributed at an average distance of 2.9 to 3.2 Å for μ varying between 0 and 4 eV. The most striking feature is that, although well defined, this layers are thicker than in the previous case, and are significantly more close-packed than the underlying O plane ($\theta \sim 4/3$, i.e. almost the density of a (111) layer).

Moreover, the analysis of the xenon planes shows that, in no case, we obtain planes identical in number and/or position to those of the oxygen or uranium ones at the surface.

All these results seem to reveal that, whatever the orientation of the UO_2 substrate, the xenon grows as a stacking of (111) planes.

3.3. UO_2 strain

We have also studied the evolution of the UO_2 layer structure as a function of the xenon chemical potential. We did not observe any additional restructuring of the UO_2 surfaces in the presence of Xe, whatever the chemical potential used, which is consistent with the results of [11]: the restructuring of the UO_2 surfaces is essentially driven by the Coulomb forces and little affected by the presence of other species.

However, the presence of Xe leads to a pressurization of the UO_2 surface and therefore, *a priori*, to a contraction of the latter in the direction perpendicular to the surface. In order to clarify these results, and in particular the effect of strains related to the presence of Xe on the UO_2 slabs, we were particularly interested in the evolution of the U-U and O-O interplane distances as a function of the chemical potential.

Let us first consider the (111) orientation. We observe that the interlayer distance decreases as μ increases, and in the same amount for all the atomic layers. More precisely, we can fit linearly this μ dependency of the interlayer distance $d_{s=111}$ as:

$$d_s = d_s^0(1 - a_s\mu) \tag{9}$$

The found values of d_s^0 and a_s are tabulated in table 2.

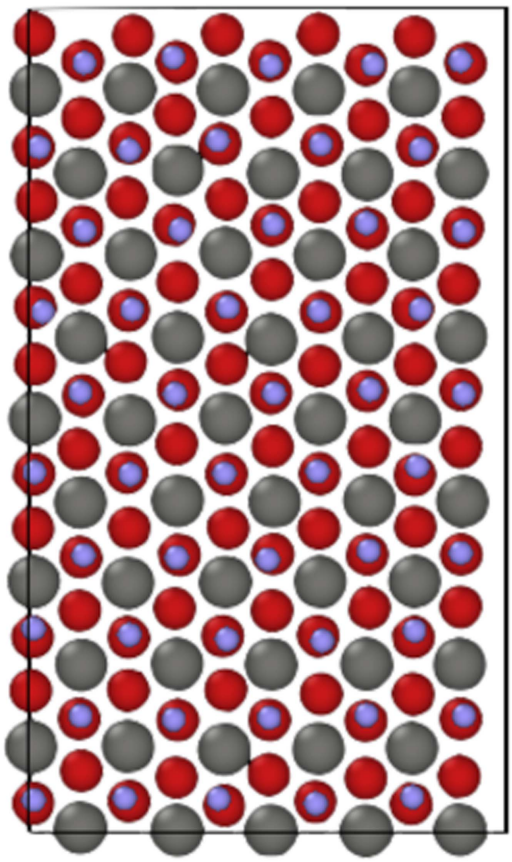

Figure 5. Structuring of the interfacial xenon plane identical to neighbouring oxygen and uranium ones, obtained after adsorption on a (111) surface, at 300 K and $\mu = 4$ eV. O atoms in red, U atoms in grey and Xe in purple.

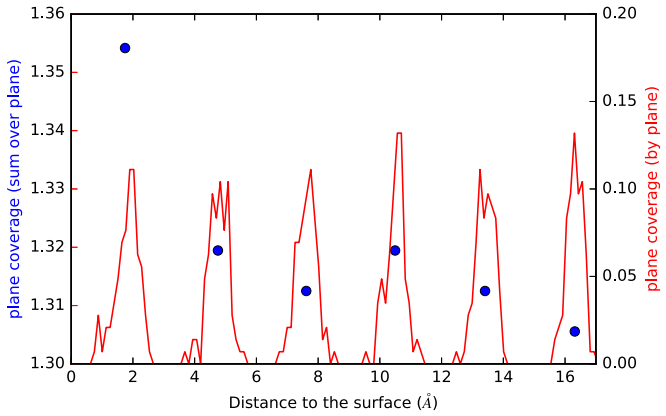

Figure 6. Xe adsorption at 1200 K and $\mu = 4$ eV on (100) UO_2 surface: Xe atomic distribution as a function of the azimuthal position. Only half of the slab is shown.

Table 2. Parameters of the equation (9) for the (111) and the (100) surfaces. d_s^0 are given in Å.

		(111)		(100)	
		d_{111}^0	a_{111}	d_{100}^0	a_{100}
U-U	Bulk	3.20	0.009	2.75	0.007
	Surface	3.21	0.009	2.97	0.011
O-O	Bulk	1.60	0.010	2.73	0.006
	Surface	1.65	0.011	2.32	0.011

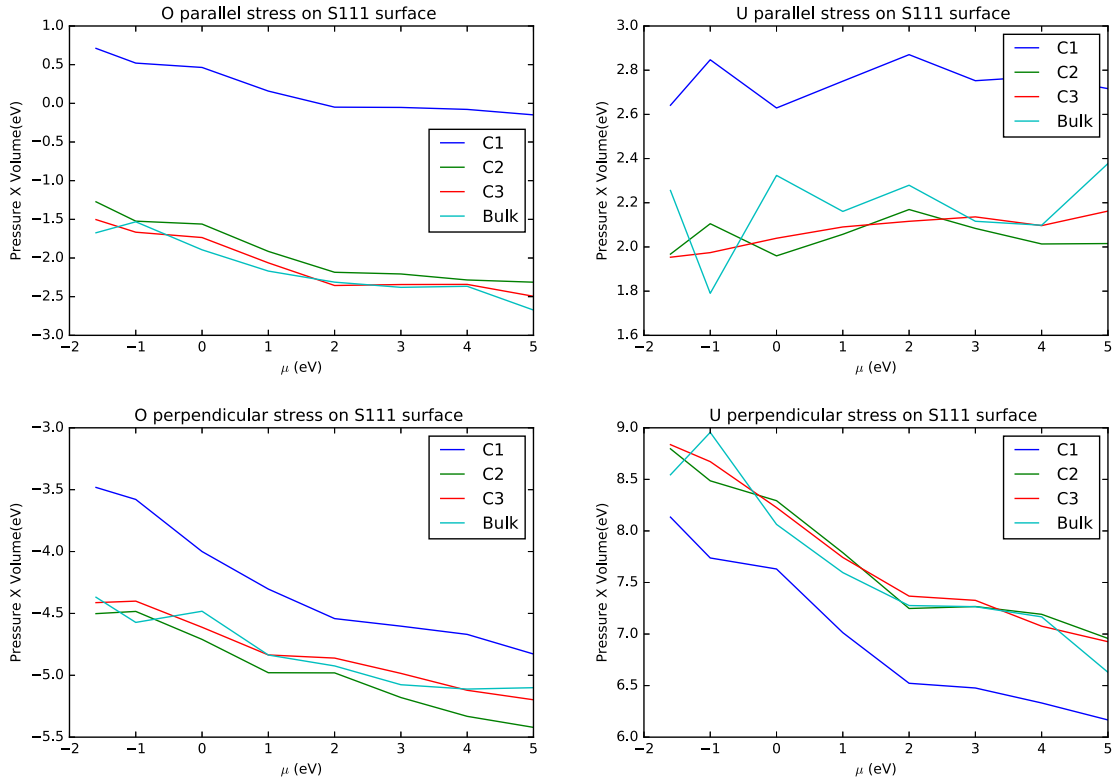

Figure 7. Stress tensor components $S_{//}$ and $S_{\perp}$ for oxygen and uranium atoms for the (111) surface, as a function of the chemical potential of xenon. Comparison between the different layers.

We can also notice, as in [11], that the dilation of the outermost (OUO) trilayer ($d^0_{111} = 1.65$ Å), compared to its bulk value ($d^0_{111} = 1.60$ Å) decreases with μ.

Concerning the (100) orientation we observe a similar decreasing linear behaviour of the interlayer distance $d_{s=100}$ as a function of μ, according equation (9), where d^0_{100} and a_{100} are tabulated in table 2. Contrary to the (111) orientation, the thickness of the surface (UO) bilayer is significantly reduced to its bulk value ($d_{100}(O_{Bulk}) > d_{100}(O_{Surface})$ whereas $d_{100}(U_{Bulk}) < d_{100}(U_{Surface})$). We can notice that the slope for the surface interlayer distance decrease is about twice as large as in the bulk. The surface planes seem to accommodate the xenon countermeasures more than the bulk ones, which are very weakly impacted.

Finally, we can compare the effect of surface orientation on the interlayer distance sensitivity to the xenon presence. The main result is that the xenon impact on the UO_2 bulk is lower for the (100) than for the (111) orientation, contrary to its impact on the UO_2 surface layer. These results seem to indicate that the surface (100), more disordered than the (111), dampens the stress induced by the xenon presence.

4. Local stress analysis

In order to clarify previous results, it is now necessary to analyse the stress levels in the xenon and the bulk, which are fundamental parameters for higher scale micromechanical models. As a reminder, the constraint analysis in the pure UO_2 surface was described in a previous work [11], which in particular highlights the importance of the electrostatic contribution and a behaviour very different between the apolar (111) and polar (100) surfaces.

4.1. (111) surface

The $S_{//}$ and $S_{\perp}$ profiles as a function of the xenon chemical potential at 1200 K are plotted on the figure 7 (O atoms on the left and U on the right). We compare the evolution of these profiles between the different layers of atoms from 'C1', the outermost layer, to the 'Bulk', i.e. the layer in the middle of the slab and exhibiting the same behaviours as an infinite perfect solid layer. First of all, we can observe that whatever the xenon chemical potential, the stress profile is rapidly damped into the bulk, only the surface layer being found to undergo a different stress from the bulk.

From this graph, we notice that the curves 'C2', 'C3' and 'Bulk' are superimposed. This confirms that only the outer part of the first triplane (OUO) is impacted by the presence of xenon. Moreover, the difference between

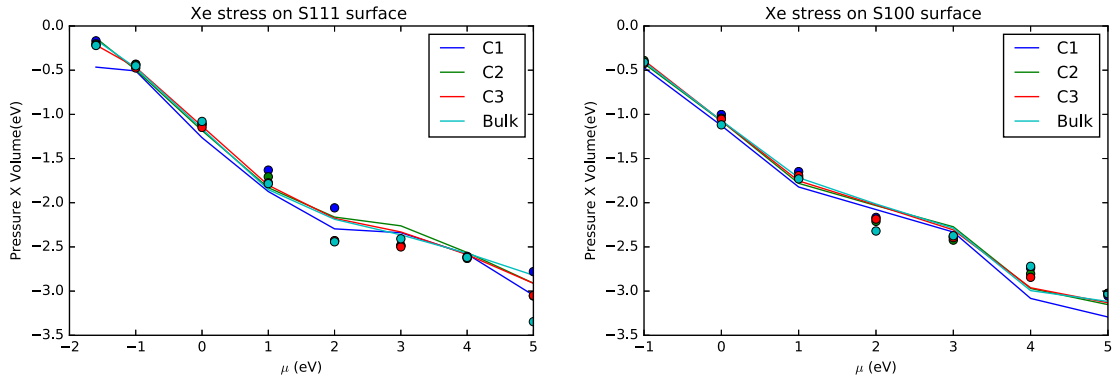

Figure 8. Stress tensor components $S_{//}$ (dots) and $S_{\perp}$ (lines) for xenon atoms adsorbed on (111) (left) and (100) (right) surfaces, as a function of the xenon chemical potential. Comparison between the different layers.

the stress in the surface plane and that in the plane of the volume leads to the measurement of the surface stress in the presence of the xenon and therefore to its evolution with the chemical potential.

4.1.1. Oxygen atoms

For the oxygen atoms, we notice that the parallel stress $S_{//}$ decreases almost linearly with the increase of the chemical potential: the oxygen atoms are all the more compressed as the xenon potential increases. The decrease of this component between the two extreme chemical potentials (-1.6 and 5 eV) is about 0.85 eV. This variation is almost identical for the different layers, which suggests that the effect of increasing the density of the xenon system has an homogeneous effect on the parallel stress. The deviation of this stress tensor component between the external surface 'C1' and that of the volume 'Bulk' leads to a surface constraint $\Delta S_{//} \sim 2.2$ eV at 1200 K independent of xenon chemical potential, and hence of xenon density.

The perpendicular stress $S_{\perp}$ also decreases almost linearly with the increase of the chemical potential. This decrease is directly attributable to the increase in the density of xenon on the surface, which induces an increase in the pressure exerted on the surface of UO_2. In contrast to $S_{//}$, the difference between this component at the external surface stress and that in the volume ($\Delta S_{\perp}$), depends on the chemical potential of the xenon: it decreases by 0.9 eV in the absence of xenon to 0.5 eV for $\mu = 5$ eV.

Thus, the first xenon effect is to compress the outermost oxygen planes as its density increases.

4.1.2. Uranium atoms

For uranium atoms, we notice that parallel stress $S_{//}$ in the different layers is almost constant with the chemical potential. This is due to the fact that uranium atoms remain almost immobile during the relaxation of the surface (after adsorption) and that they do not feel the presence of the xenon atoms, which is screened by the external oxygen layer. This observation is consistent with the fact that the parallel component of the stress tensor $\Delta S_{//}$ on the surface remains identical to its value (0.8 eV) without xenon.

The perpendicular stress of the uranium atoms decreases in a similar way (with a slope twice as great) to that of the oxygen atoms with the chemical potential (the xenon decreases the stress in tension). As for the perpendicular component of the surface stress, it remains almost constant and equal to its value ($\simeq -0.8$ eV) without xenon.

4.1.3. Xenon atoms

The stress profiles evolution as a function of the chemical potential for the different xenon atom layers is plotted in figure 8. We can see that the two components are almost identical, indicating an isotropy of the state of stress in the xenon layer.

This stress becomes more and more negative when the chemical potential increases in association with higher compression. The comparison between these profiles for the different layers shows that these quantities are independent of the distance to the surface of UO_2 (profiles are almost superimposed). It can therefore be deduced that there is no need to define a 'surface stress' in the xenon layer in the sense that we have done for the UO_2 substrate.

4.1.4. The whole system

In the figure 9, we plot the per atom total constraint $\left(\frac{Tr(S)}{3}\right)$ averaged by 'effective UO_2 layer', as a function of its azimuthal position at 1200 K for various values of the chemical potential (-1.6 and 5 eV). The effective layer for

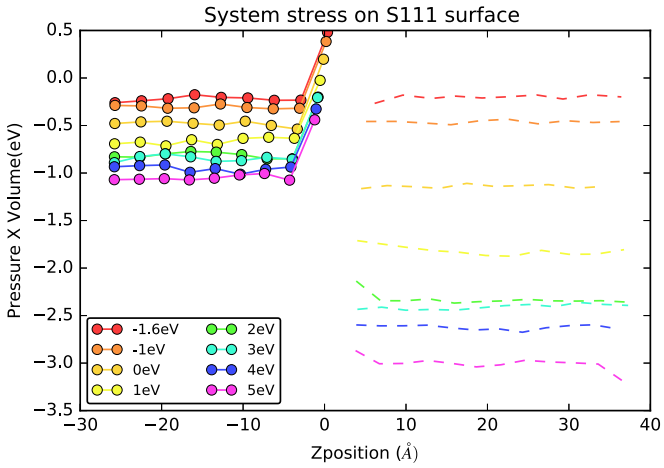

Figure 9. Average stress profile perpendicular to the (111) surfaces for the UO_2 effective layers (solid lines) and Xe ones (dashed lines), for various μ values. Each point on this figure corresponds to the stress value averaged on an atomic layer, and plotted as a function of the average distance of this layer to the surface of the slab. Only the right half of the total slab is shown.

orientation (111) refers in the UO_2 substrate to (OUO) triplanes and the xenon layer to atomic planes parallel to the surface.

We can see on this profile that the role of the interface is only sensitive to the first (OUO) triplane, which is less compressed than those of the volume. The full layer is in compression, especially at high chemical potential. This compression that results from the presence of the xenon on a layer of confined UO_2 will be useful in the perspective of implementation of our results in micromechanical codes.

4.2. (100) surface

Similarly to the (111) surface, the evolution of the perpendicular $S_\perp$ and parallel $S_{//}$ stress tensor components with the xenon chemical potential at 1200 K is plotted in figure 10, for the O (left) and U (right) atoms and for the different atom layers of the (100) surface.

It can be seen in this figure that, unlike the (111) surface, it is the stress state in the first two atomic planes of both U and O that differs significantly from that of volume and remains non-negligible in the third plane. Thus, as in our analysis of the (100) surface without xenon [11], we find that the first two planes of uranium and oxygen are perturbed by the presence of the surface, and remain so, even in the presence of xenon.

4.2.1. Oxygen atoms

For the oxygen atoms, similarly to the (111) surface, the parallel stress component $S_{//}$ decreases as the chemical potential increases. The decrease of this component between extreme chemical potentials (-1 and 5 eV) or the surface layer (C1), about 0.85 eV, is higher than that of (111) surface (about 0.65 eV in this range). We can also notice that the bulk stress component $S_{//}(Bulk)$ remains almost constant in this range of chemical potential. The perpendicular stress component $S_\perp$ also decreases with the chemical potential increase, but here, this linear decrease seems to affect all the oxygen layers until the bulk.

4.2.2. Uranium atoms

Concerning the uranium atoms, contrary to the (111) surface, the $S_{//}(C1)$ component decrease with the xenon chemical potential increase is high (about 1.1 eV) whereas it remains almost null for the internal layers. The surface stress $S_\perp$ also decreases according to the chemical potential from 5 to 4.2 eV. As for oxygen, the stresses in the second and third plane of uranium vary in the same order of magnitude.

4.2.3. Xenon atoms

In figure 8 (right), we plot the stress evolution as a function of the chemical potential for the different xenon atom layers. From the first observation, we can notice that a very similar behaviour to the one of the (111) surface is observed, namely that the two parallel and perpendicular components are quasi-identical, which is the signature of an isotropic state of stress in the xenon layer. Moreover, the orders of magnitude are the same for the two surfaces, which indicates that the stress in the xenon layer does not depend on the orientation of the substrate of UO_2 on which it is adsorbed.

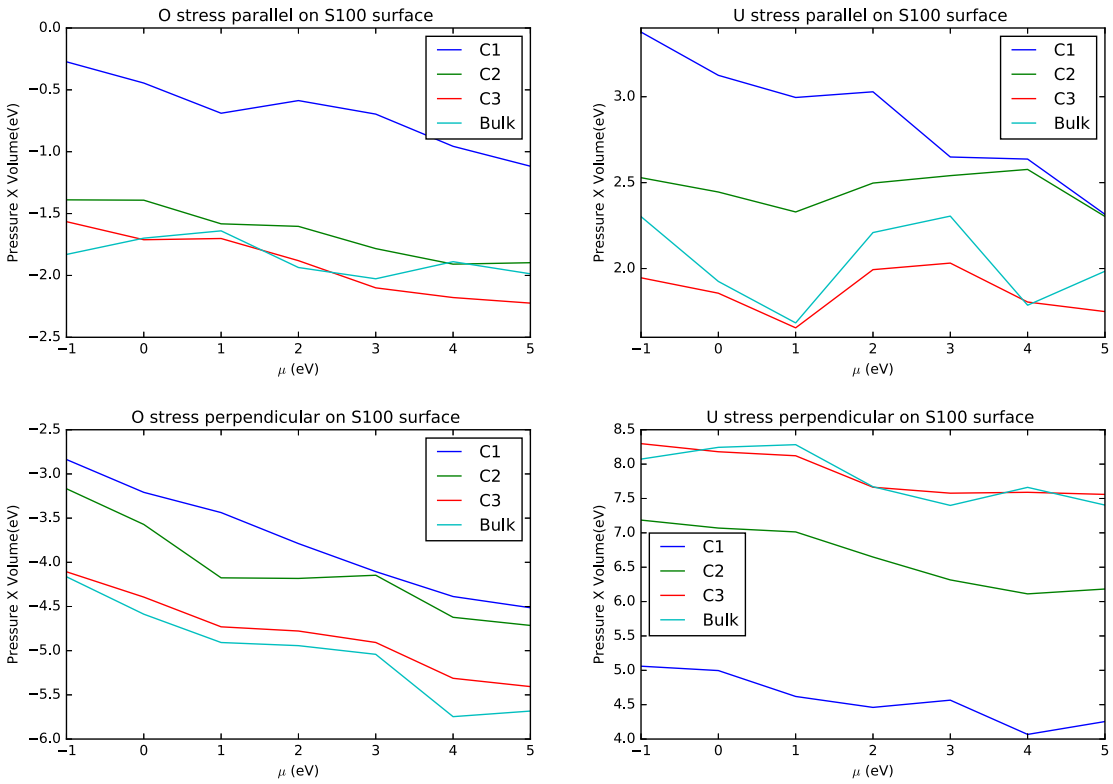

Figure 10. Stress tensor components $S_{//}$ and $S_{\perp}$ for oxygen and uranium atoms of (100) surface, as a function of the chemical potential of xenon. Comparison between the different layers.

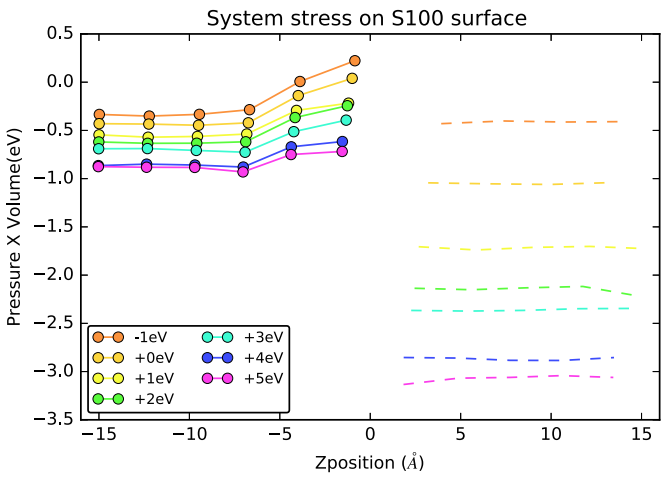

Figure 11. Average stress profile perpendicular to the (100) surfaces for the UO_2 effective layers (solid lines) and Xe ones (dashed lines), for various μ values. Each point on this figure corresponds to the stress value averaged on an atomic layer, and plotted as a function of the average distance of this layer to the surface of the slab.

4.2.4. The whole system

In the figure 11, we plot the total per atom stress $\left(\frac{Tr(S)}{3}\right)$ averaged by 'effective UO_2 layer', perpendicular to the UO_2/Xe, at 1200 K, for various values of the chemical potential (−1.6 and 5 eV). The effective layer for orientation (100) refers in the UO_2 substrate to the (1/2 O—U—1/2 O) triplanes for bulk layers and (O—U—1/2 O) for surface layer to ensure stoichiometry.

We can see on this profile that the role of the interface is only sensitive to the two first layers of UO_2, which are less compressed than those of the volume. The full layer is in compressive stress, especially at high chemical potential.

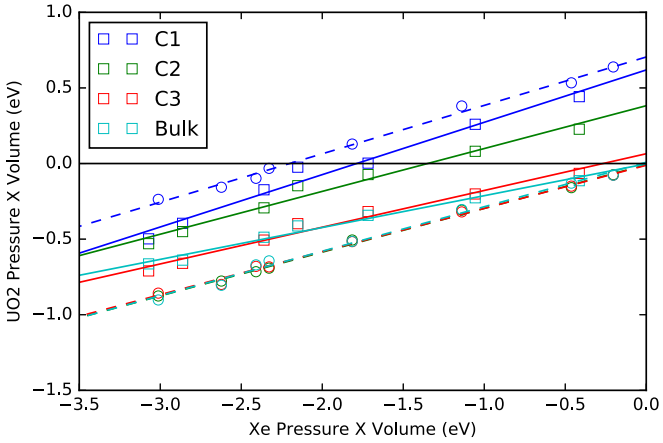

Figure 12. Average stress profile perpendicular to the (100) (squares) and the (111) (circles) surfaces for the UO_2 effective layers as a function of the Xe ones, for various layers. The reference stress state is the bulk one, for zero pressure of xenon.

4.3. Discussion

As illustrated in figure 12, we can summarize all the previous results by a quite different behaviour of the UO_2 surface as a function of its orientation: in the (111) surface, only the first surface layer is affected by the presence of the xenon, and the per atom stress evolves linearly with the xenon one. For the (100) surface, the xenon stress impact is converged only above the fourth layer, and the stress that is viewed by the bulk layers is lower than in the (111) case. The (100) surface leads to a more efficient damping, which can be connected and imputed to a greater accommodation of the surface due to its initial disorder.

5. Conclusion

We have presented here a theoretical study of xenon incorporation in UO_2 (111) and (100) surfaces, by mean of GCMC approaches based on semi-empirical potentials. The corresponding results allowed us to highlight the following points.

During Xenon incorporation in an empty box or xenon adsorption on UO_2 surfaces, we observed a phase transition from a diluted to dense phase. The adsorption isotherms depend on the temperature of the system and the chemical potential of the xenon but are independent of the surface presence. The dense phase of xenon has a complex structure with the coexistence of BCC and FCC phases, and adopts a (111) stacking perpendicular to the UO_2 surface, whatever its orientation ((111) or (100)). This highly compressed layered structure of xenon develops from a pseudomorphic interface in the case of UO_2 (111) and a disordered interface buffer layer in the case UO_2 (100).

The mechanical analysis of the surfaces after xenon adsorption revealed a decrease in the stress of oxygen and uranium atoms induced by the presence of xenon on the UO_2 surfaces. This decrease is all the more important as the density of the xenon atom increases. It can also be noted that the difference between the stresses of the surface layer and the bulk increases with the chemical potential in the case of the (100) surface but remains constant in the case of the (111) surface, which seems to indicate that the surfaces (100) make it possible to better mitigate the xenon pressurization and to limit the stresses in the matrix, most probably due to its structural disorder. It would obviously be interesting to compare the results that we have just summarized with experimental data and/or other theoretical works. Unfortunately, the only reported experimental observations concern bubbles included in matrices and not surfaces. Moreover, at least to our knowledge, there are no other calculations performed on systems studied here, either in DFT or using semi-empirical potentials. These results should now be introduced in advanced micromechanical models, which should take into account the different behaviours associated to each surface orientation, for instance using various effective surface thickness and surface tension values.

Acknowledgments

The authors are indebted to C Garnier for useful discussion and the company AREVA for its financial support.

ORCID iDs

Fabienne Ribeiro https://orcid.org/0000-0001-6492-2678

References

[1] Martin P, Garcia P, Carlot G, Sabathier C, Valot C, Nassif V, Proux O and Hazemann J-L 2008 Xas characterisation of xenon bubbles in uranium dioxide *Nuclear Instruments and Methods in Physics Research section B: Beam Interactions with Materials and Atoms* **266** 2887–91

[2] Garcia P *et al* 2006 A study of xenon aggregates in uranium dioxide using x-ray absorption spectroscopy *J. Nucl. Mater.* **352** 136–43

[3] Castell M R 2003 Wulff shape of microscopic voids in UO_2 crystals *Phys. Rev.* B **68** 235411

[4] Vincent P-G, Monerie Y and Suquet P 2009 Porous materials with two populations of voids under internal pressure: I. Instantaneous constitutive relations *Int. J. Solids Struct.* **46** 506

[5] Alba-Simionesco C, Coasne B, Dosseh G, Dudziak G, Gubbins K E, Radhakrishnan R and Sliwinska-Bartkowiak M 2006 Effects of confinement on freezing and melting *Journal of Physical-Condensed Matter* **82** R15–68

[6] Jelea A *et al* 2014 An atomistic modeling of the xenon bubble behavior in the UO_2 matrix *J. Nucl. Mater.* **444** 153–60

[7] Parfitt D C and Grimes R W 2008 Predicted mechanisms for radiation enhanced helium resolution in uranium dioxide *J. Nucl. Mater.* **381** 216–22

[8] Xiao-Feng T, Chong-Sheng L, Zheng-He Z and Tao G 2010 Molecular dynamics simulation of collective behaviour of xe in UO_2 *Chin. Phys.* B **19** 057102

[9] Cagna C, Zacharie-Aubrun I, Bienvenu P, Barrallier L, Michel B and Noirot J 2016 A complementary approach to estimate the internal pressure of fission gas bubbles by sem-sims-epma in irradiated nuclear fuels *IOP Conf. Series: Materials Science and Engineering* **109** 012002 In IOP, editor

[10] Colbert M, Tréglia G and Ribeiro F 2014 Theoretical study of xenon adsorption in uo2 nanoporous matrices *J. Phys.: Condens. Matter* **26** 485015

[11] Arayro J, Tréglia G and Ribeiro F 2015 Atomistic modelling of residual stress at uo2 surfaces *J. Phys.: Condens. Matter* **28** 015006

[12] Govers K 2008 Atomic scale simulations of noble gases behaviour in uranium dioxide *PhD Thesis* Université Libre de Bruxelles

[13] Leach A R 1996 *Molecular Modelling : Principles and Applications* (Upper Saddle River, NJ: Prentice Hall)

[14] Catlow C R A 1977 Ion transport and interatomic potentials in the alkaline-earth-fluoride crystals *J. Phys. C: Solid State Phys.* **10** 1627

[15] Jackson R A and Catlow C R A 1985 Trapping and solution of fission Xe in UO_2 *J. Nucl. Mater.* **127** 161–6

[16] Grimes R W *et al* 1991 The stability of fission products in uranium dioxyde *Philosophical Transactions of the Royal Society of London. Series A: Physical and Engineering Sciences* **335** 609–34

[17] Sattonnay G and Tétot R 2013 Bulk, surface and point defect properties in UO_2 from a tight-binding variable-charge model *J. Phys.: Condens. Matter* **25** 125403

[18] Basak C B, Sengupta A K and Kamath H S 2003 Classical molecular dynamics simulation of UO_2 to predict thermophysical properties *J. Alloys Compd.* **360** 210–6

[19] Geng H Y, Chen Y, Kaneta Y and Kinoshita M 2008 Molecular dynamics study on planar clustering of xenon in UO_2 *J. Alloys Compd.* **457** 465–71

[20] Jelea A, Colbert M, Ribeiro F, Tréglia G and Pellenq R J M 2011 An atomistic modelling of the porosity impact on UO_2 matrix macroscopic properties *J. Nucl. Mater.* **415** 210–6

[21] Basak C B, Sengupta A K and Kamath H S 2003 Classical molecular dynamics simulation of uo 2 to predict thermophysical properties *J. Alloys Compd.* **360** 210–6

[22] Brearley I R and MacInnes D A 1980 An improved equation of state for inert gases at high pressures *J. Nucl. Mater.* **95** 239–52

[23] Jelea A, Colbert M, Ribeiro F, Treglia G and Pellenq R J-M 2011 An atomistic modelling of the porosity impact on uo 2 matrix macroscopic properties *J. Nucl. Mater.* **415** 210–6

[24] Plimpton S 1995 Fast Parallel Algorithms for Short-Range Molecular Dynamics *J. Comp. Phys.* **117** 1–19

[25] Heyes D M 1994 Pressure tensor of partial-charge and point-dipole lattices with bulk and surface geometries *Phys. Rev.* B **49** 755

[26] Nicoll S, Matzke H J and Catlow C R A 1995 A computational study of the effect of xe concentration on the behaviour of single xe atoms in uo2 *J. Nucl. Mater.* **226** 51–7

[27] Govers K, Lemehov S E and Verwerft M 2010 On the solution and migration of single xe atoms in uranium dioxide-an interatomic potentials study *J. Nucl. Mater.* **405** 252–60

[28] Aprile E 2006 *Noble gas Detectors* (New York: Wiley)

[29] Stukowski A 2010 Visualization and analysis of atomistic simulation data with ovito—the open visualization tool *Modelling Simul. Mater. Sci. Eng.* **18** 015012

[30] Belonoshko A B 2008 Triple fcc-bcc-liquid point on the xe phase diagram determined by the n-phase method *Phys. Rev.* B **78** 174109

[31] Desgranges C and Delhommelle J 2008 Crystallization mechanisms for supercooled liquid xe at high pressure and temperature: hybrid monte carlo molecular simulations *Phys. Rev.* B **77** 054201

[32] Geng H Y, Chen Y, Kaneta Y and Kinoshita M 2008 Molecular dynamics study on planar clustering of xenon in uo 2 *J. Alloys Compd.* **457** 465–71